https://doi.org/10.5194/egusphere-2026-3451
Preprint. Discussion started: 29 June 2026

Extratropical interactions with the tropical moist margin: a case study and the role of latent heating

Corey Robinson[1,2,3], Sugata Narsey[4], Bethan White[5,2], Chermelle Engel[6], Paul Gregory[5,2], and Christian Jakob[1,2]

[1]School of Earth, Atmosphere & Environment, Monash University, Clayton, Australia
[2]ARC Centre of Excellence for 21st Century Weather, Monash University, Clayton, Australia
[3]Department of Meteorology, University of Reading, Reading, UK
[4]Bureau of Meteorology, Melbourne, Australia
[5]School of Geography, Earth and Atmospheric Sciences, University of Melbourne, Melbourne, Australia
[6]ACCESS-NRI, Australian National University, Canberra, Australia

Correspondence: Corey Robinson (c.robinson@reading.ac.uk)

Abstract. The tropical moist margin occasionally extends into the extratropics, where it can lead to heavy precipitation in otherwise dry regions. Here, we examine the physical processes involved in these events and their interaction with the extratropical flow. Employing tools such as budget and trajectory analysis, we analyse a case study of an extratropical interaction with the moist margin in January 2018. This event produces a subtropical cyclone and results in damaging winds and precipitation over New Zealand. The event is then simulated with the ACCESS-rAM3 model, highlighting the critical role of latent heating in the development of the cyclone. Overall, the results suggest that interactions between extratropical PV and the moist margin occur in both directions. Deep cyclonic PV anomalies of upstream extratropical origin can result in poleward moisture advection leading to poleward displacement of the moist margin, while convection inside a perturbed moist margin can lead to upper-level ridge building through poleward advection of anticyclonic PV by the divergent wind. These results have implications for the diagnosis and prediction of severe weather, especially for extreme precipitation in the subtropics.

1 Introduction

The tropical moist margin provides a simple diagnostic for rainfall in tropical regions (Mapes et al., 2018). Defined as a contour of constant total column water vapour, it encloses the majority of precipitation over tropical oceans and some land regions, and its movement on daily time scales is strongly related to precipitation variability (Robinson et al., 2024).

The movement of the moist margin is related to a variety of weather systems, such as convectively coupled equatorial waves, the Madden-Julian Oscillation, and low-pressure systems (Robinson et al., 2025). In particular, there exists a strong relationship between the moist margin and extratropical potential vorticity (PV) anomalies on the 350 K isentropic surface, in

https://doi.org/10.5194/egusphere-2026-3451
Preprint. Discussion started: 29 June 2026

which poleward displacement of the margin occurs in locations near upper-level anticyclonic PV anomalies. These events can produce long-lived and heavy precipitation over a large area extending from the tropics to the extratropics.

The overall aim of this study is to examine the physical processes during interactions between the moist margin and extratropical PV anomalies in more detail. Cyclonic PV anomalies are representative of upper-level troughs, which can destabilise the atmosphere, leading to convection (Juckes and Smith, 2006), and can serve as a precondition for surface cyclones through baroclinic instability (Barnes et al., 2021b; Pierrehumbert and Swanson, 1995; Hoskins et al., 1985). Due to the associated cyclonic circulation around the PV anomaly, moist advection and poleward movement of the moist margin may occur along the eastern flank of the PV anomaly.

Anticyclonic PV anomalies are representative of upper-level ridges, with persistent events often described as “blocking”. Recent literature has highlighted the role of diabatic processes in the development of upper-level ridges and blocks (Hauser et al., 2023; Steinfeld et al., 2020; Steinfeld and Pfahl, 2019; Pfahl et al., 2015). Particularly notable examples of this occur due to condensation in the warm-conveyor belts of extratropical cyclones (Methven, 2014; Saffin et al., 2021) or tropical cyclones transitioning into the extratropics (Torn, 2010; Keller et al., 2019). This occurs due to the poleward advection of anticyclonic PV through the upper-level divergent flow above the region of precipitation. Therefore, we may also expect convection that occurs near the edge of a poleward-perturbed moist margin to contribute to the development of upper-level anticyclonic PV anomalies.

In this work, we propose that interactions between the moist margin and extratropics occur in both directions. The role of upper-level PV anomalies on the moist margin is to draw tropical moisture poleward on the eastern flank of the upper-level cyclone, moistening and destabilising the column and leading to precipitation. The convection located near the edge of the perturbed moist margin feeds back onto the upper-level PV by contributing to ridge building, and possibly further downstream development. To test this hypothesis, we examine a case study of an interaction between the moist margin and extratropics that occurred near New Zealand in January 2018. The case is examined in the ERA5 reanalysis with a combination of Eulerian and Lagrangian tools, such as the moisture budget, PV budget and trajectory analysis. The role of diabatic processes is tested with a suite of model experiments with modified latent heating strength.

The remainder of the paper is structured as follows. Section 2 outlines the data and methodologies, including the experimental setup of the model. In Section 3 we examine the development of the event in the ERA5 reanalysis, including moisture budget and trajectory analysis. The results of the latent heating are presented in Section 4. A discussion and conclusion are provided in Section 5.

2 Methods & Data

2.1 Data

The case study is analysed using data from the European Centre for Medium- Range Weather Forecasts ERA5 reanalysis Hersbach et al. (2020). We use hourly data for mean sea-level pressure (MSLP), total column water vapour (TCWV), evaporation, precipitation, potential vorticity (PV), horizontal and vertical winds, specific humidity, temperature, and geopotential at 0.25°

resolution. Data on pressure levels are taken on 27 levels between 100 and 1000 hPa, and isentropic PV is taken on the 350 K surface.

2.2 Cyclone tracking

Cyclone tracking is performed with version 2 of the TempestExtremes algorithm (Ullrich et al., 2021). The algorithm detects the cyclone as a point-wise local minimum in mean sea level pressure every 6 hours and connects these in time as tracks.

2.3 Moisture and potential vorticity budgets

Two quantities of interest in this study are the total column water vapour (TCWV) and potential vorticity (PV), so it is pertinent to apply budgets to understand changes in these quantities. The column-integrated moisture budget can be written as:

$$\frac{d\langle q\rangle}{dt} = -\nabla_h \cdot \langle \mathbf{u_h} q\rangle + E - P \tag{1}$$

Here, q is the specific humidity, $\mathbf{u_h}$ is the horizontal wind vector, ∇_h is the horizontal gradient operator, and E and P are the surface evaporation and precipitation fluxes, respectively. Angled brackets denote a mass-weighted vertical integral from the surface p_s to the top of the atmosphere p_t defined as $\langle\cdot\rangle = \frac{1}{g}\int_{p_s}^{p_t} \cdot \, dp$, noting that the total column water vapour can hence be written as $\langle q\rangle$. Equation 1 states that changes in TCWV occur through horizontal flux convergence of moisture, evaporation, and precipitation. Furthermore, the flux convergence $-\nabla_h \cdot \langle \mathbf{u_h} q\rangle$ can be separated into convergence and advection through the vector identity $-\nabla_h \cdot \langle \mathbf{u_h} q\rangle = -\langle q \nabla_h \cdot \mathbf{u_h}\rangle - \langle \mathbf{u_h} \cdot \nabla_h q\rangle$.

It is important to note that since TCWV is a vertically integrated quantity, vertical motion does not directly contribute to column moistening or drying. However, vertical motion is associated with horizontal convergence from the continuity equation, meaning a vertical advection term is sometimes included. This is common in moist static energy budgets. In this study, we choose to keep all dynamical terms in the horizontal direction to avoid ambiguity.

The tendency equation for potential vorticity PV, is:

$$\frac{d(PV)}{dt} = \frac{(f\mathbf{k} + \nabla \times \mathbf{u}) \cdot \nabla \dot{\theta}}{\rho} \tag{2}$$

On the 350 K isentropic surface, ERA5 heating data suggest that direct modification of PV by $\dot{\theta}$ is minimal (not shown). Therefore, PV is materially conserved and is simply advected by the wind:

$$\frac{\partial(PV)}{\partial t} = -\mathbf{u} \cdot \nabla PV \tag{3}$$

Insight into processes that change PV can be gained by partitioning the wind into different components, following Teubler and Riemer (2016). We opt for a simple decomposition into rotational and divergent components, achieved with a Helmholtz decomposition. Teubler and Riemer (2016) further decompose the rotational part of the wind into “quasi-barotropic” and “baroclinic” components through a piecewise PV inversion. We do not opt for this due to the complexity of PV inversion, especially at lower latitudes, and since the principal focus of this study is on the divergent wind. Mathematically, this is

https://doi.org/10.5194/egusphere-2026-3451
Preprint. Discussion started: 29 June 2026

represented by:

$$\frac{\partial P}{\partial t} = -\left(\mathbf{u}_\psi + \mathbf{u}_\chi\right) \cdot \nabla P \tag{4}$$

Here, $\mathbf{u}_\psi$ and $\mathbf{u}_\chi$ are the rotational and divergent parts of the wind, respectively. Note that the Helmholtz partitioning is non-trivial over a limited domain. Here, we use a successive over-relaxation method and select boundary conditions to minimise the kinetic energy of the divergent wind, following Lynch (1989).

We also split the PV into a background and an anomalous component. Given the limitations of a regional simulation, we take the background to be the time-longitude mean of PV across the whole domain and the simulation duration.

2.4 Trajectory analysis

In this study, we use version 2.0 of the LAGRANTO analysis tool (Sprenger and Wernli, 2015) to calculate back trajectories from various regions of interest. Trajectories are calculated over 96 hours with a horizontal spacing of 0.5°, and are evaluated with hourly ERA5 data at 0.25° resolution. ERA5 data for pressure, potential temperature, specific humidity, relative humidity, TCWV and PV are also extracted along trajectories. Note that TCWV is a column-integrated quantity, so its traced value refers to the TCWV at the latitude-longitude position of the air parcel regardless of its pressure level.

2.5 ACCESS-rAM3 experimental setup

We use the ACCESS-rAM3 model, which is a regional coupled land-atmosphere model based on the UK Met Office regional nesting suite designed for use on the National Computational Infrastructure (NCI) in Australia. The atmospheric component of the model is version 13.5 of the Unified Model (UM) (Brown et al., 2012), while the land component is version 7.5 of the Joint UK Land Environment Simulator (JULES) (Best et al., 2011; Clark et al., 2011). We set up the model at 0.1° resolution (∼11 km) over a domain covering 120-210°E, 5-65°S. The simulation is run with the Global Atmosphere/Land 9.0 (GAL9) science configuration, which notably contains a mass flux convection scheme (Walters et al., 2019; Willett et al., 2026). The vertical resolution consists of 70 hybrid-height levels up to 80 km.

The model is initialised on 12Z 01 January 2018 with ERA5 and ERA5-Land initial and boundary conditions (Hersbach et al., 2020; Muñoz-Sabater et al., 2021), and is run for 7 days, covering the entirety of the event. An advantage of the ACCESS-rAM3 setup is that ERA5-land soil moisture, soil temperature and skin temperature are included at the native resolution of 0.1°, rather than downscaled from 0.25°, which is important for the accuracy of runs (Ayat et al., 2025). Sea surface temperatures are supplied by the ERA5 skin temperature variable, and held constant throughout the simulation for simplicity. The model is free-running in the interior, and the lateral boundary conditions are updated every hour. A summary of the model configuration is provided in Table 1.

Initial runs using the GAL9 science configuration on this domain revealed large spikes in total precipitation that occurred every 24 hours. These spikes were traced to the reset of the convective prognostic precipitation variable in the GAL9 reconfiguration task to a constant value. This reconfiguration task was run daily to update values of soil moisture within the forecast domain.

Table 1. ACCESS-rAM3 model configuration for the case study.

Horizontal resolution	0.1°
Vertical resolution	70 hybrid-height levels up to 80 km
Simulation time	12Z 01-08 January 2018
Cycling	Free-running
Science settings	GAL9 (Willett et al., 2026)
Initial & boundary conditions	ERA5 (Hersbach et al., 2020) & ERA5-Land (Muñoz-Sabater et al., 2021)
Sea surface temperatures	Constant climatology

Our solution was to create two GAL9 configuration files. One configuration file was called for the first cycle of the forecast to reconfigure all the ERA5 driving model variables onto the forecast domain, while the second configuration file (with the constant value of convective prognostic precipitation removed) was used for all subsequent, free-running cycles."

Experiments with modified latent heating are performed by multiplying the constants for the latent heat of condensation (L_c) and fusion (L_f) of water by factors 0.5, 0.75, 1.25 and 1.5, along with a control simulation where they are unchanged. Notably, this means that any process that causes changes of state in water between solid, liquid and gaseous forms will result in a different amount of energy being absorbed or released, regardless of which component of the model it occurs in.

3 ERA5 analysis of case study

3.1 Synoptic-dynamic structure and evolution

Figure 1 shows the evolution of the cyclone track in ERA5. The system is first detected off the coast of eastern Australia late on 18Z 02 January with a minimum MSLP of 1000 hPa. The low moves south-eastward and intensifies, reaching a minimum pressure of 977 hPa on 18Z 04 January. After crossing New Zealand on 05 January, the system weakens slightly and subsequently reintensifies after moving offshore, stalling somewhat near the dateline. From 07 January onward, the system weakens as it tracks eastward.

The synoptic evolution of the event is presented in daily snapshots every 12Z from 01-06 January 2018 in Figures 2 and 3. On 01 January (panels a-b), there is a weak inverted trough over eastern Australia and weak pressure gradients over the Tasman Sea. The moist margin is already perturbed poleward over the east coast of Australia with some scattered rainfall near its boundary. This moisture is due to a tropical cyclone-front interaction over northwest Australia in previous days, with moisture directed towards the Coral Sea by an upper-level anticyclone over central-eastern Australia (not shown). The PV structure shows a trough to the east and a ridge to the west of the moist margin perturbation. A similar structure is evident on 02 January (panels c-d) with the moist margin expanding slightly eastward. A region of strong precipitation is evident along the eastern coast of Australia. An upper-level cyclone approaches from south-eastern Australia, also evident by the 500 hPa trough

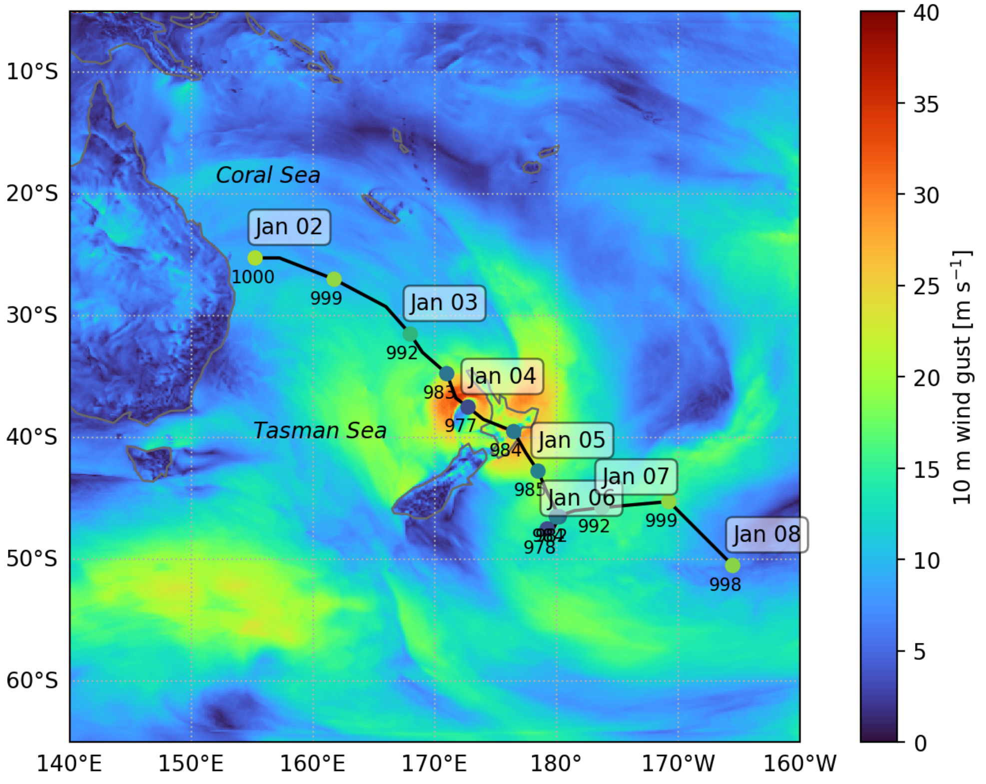

Figure 1. Track of the cyclone in ERA5 as determined by TempestExtremes algorithm. Minimum mean sea-level pressure are annotated every 12 hours in hPa, and times are annotated daily at 18Z. Overlaid are the wind gusts from the control experiment in ACCESS-rAM3 at 18Z 04 January 2018, close to the time of maximum intensity.

in geopotential height. Note that although the interaction with the extratropics has not yet occurred, the poleward displacement of the moist margin is presumably an important precondition for the interaction in the following days.

The interaction with the extratropics becomes more evident on 03 January (Figure 2, panels e-f). At this time, the moist margin shifts substantially southward toward New Zealand. Meanwhile, a low-pressure system begins to form around 165E, 30S, although there are no closed contours in the 500 hPa geopotential height. The PV shows a clear wave-like structure with a prominent upper-level cyclonic anomaly to the west and a developing upper-level anticyclone at similar longitudes to the moist margin perturbation.

From here, the cyclone rapidly intensifies, with closed contours in both MSLP and 500 hPa geopotential height. The moist margin perturbation is stretched into a narrower band ahead of the cyclone on 04 January (Figure 3, panels a-b). Meanwhile, the upper-level anticyclone becomes more prominent, extending poleward of 40S. The PV structure begins to overturn cyclonically, indicating Rossby wave breaking. Note that at this time, most of the cyclone-related precipitation now falls outside the moist margin. This is likely due to precipitative drying and lack of moisture resupply by the circulation in a colder, drier atmosphere.

https://doi.org/10.5194/egusphere-2026-3451
Preprint. Discussion started: 29 June 2026

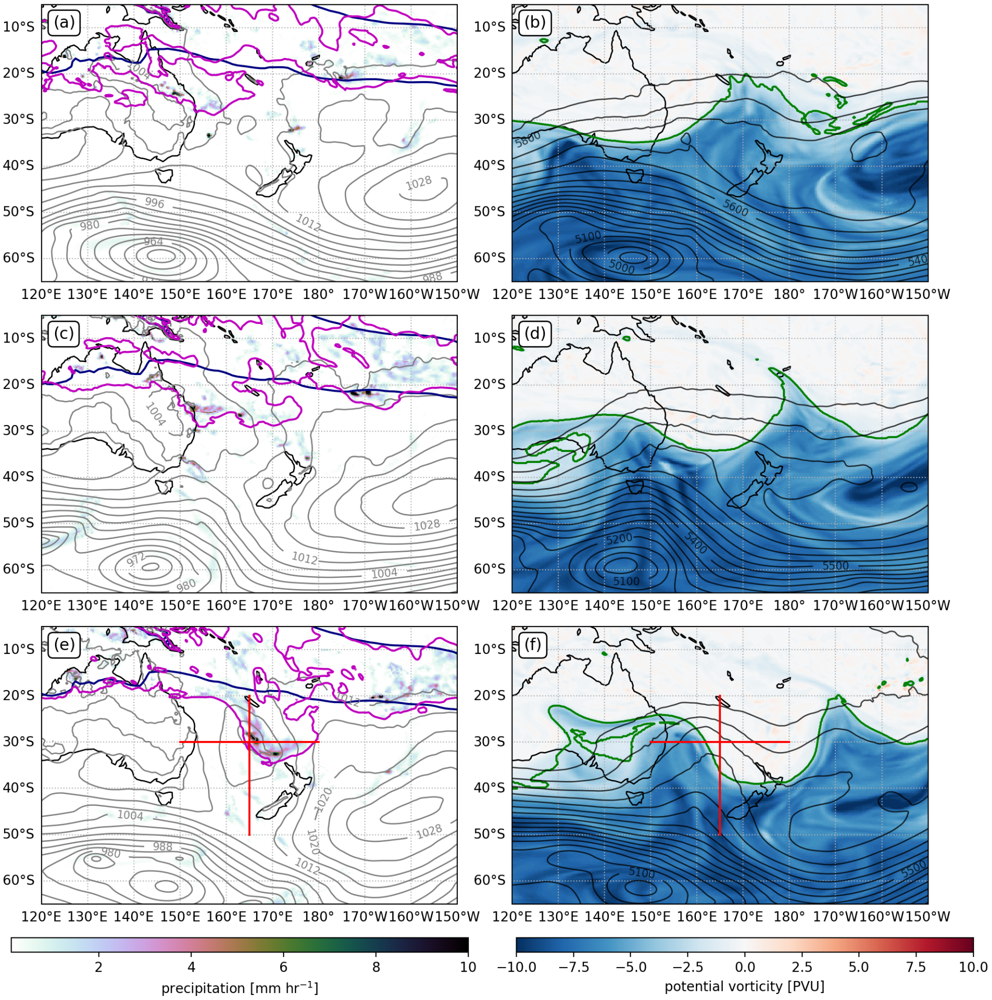

Figure 2. ERA5 synoptic plots for 12Z 01 January (a-b), 12Z 02 January (c-d), and 12Z 03 January (e-f). Plotted are (a, c, e) mean sea level pressure in contours every 4 hPa, precipitation rate in shading, and the current and climatological moist margin in magenta and clue contours respectively; and (b, d, f) 350 K potential vorticity in shading, 500 hPa geopotential height in contours. The red lines in panels e-f denote the location of cross-sections in Figure 4.

The moist margin is also a weaker predictor of precipitation at higher latitudes, as discussed in Robinson et al. (2024). Despite this, we hypothesise that the initial moist margin perturbation during 01-03 January is necessary for the interaction to occur.

On 05 January, the cyclone weakens slightly after crossing New Zealand, and is also less prominent at 500 hPa. The moist 150 margin is now well clear of the cyclone and returning towards the tropics. However, the PV structure has amplified and cyclonic Rossby wave breaking is more apparent. By 06 January, the cyclone re-intensifies to a minimum surface pressure of 978 hPa and consists of multiple closed contours in the 500 hPa geopotential height. A large upper-level cyclone exists around New

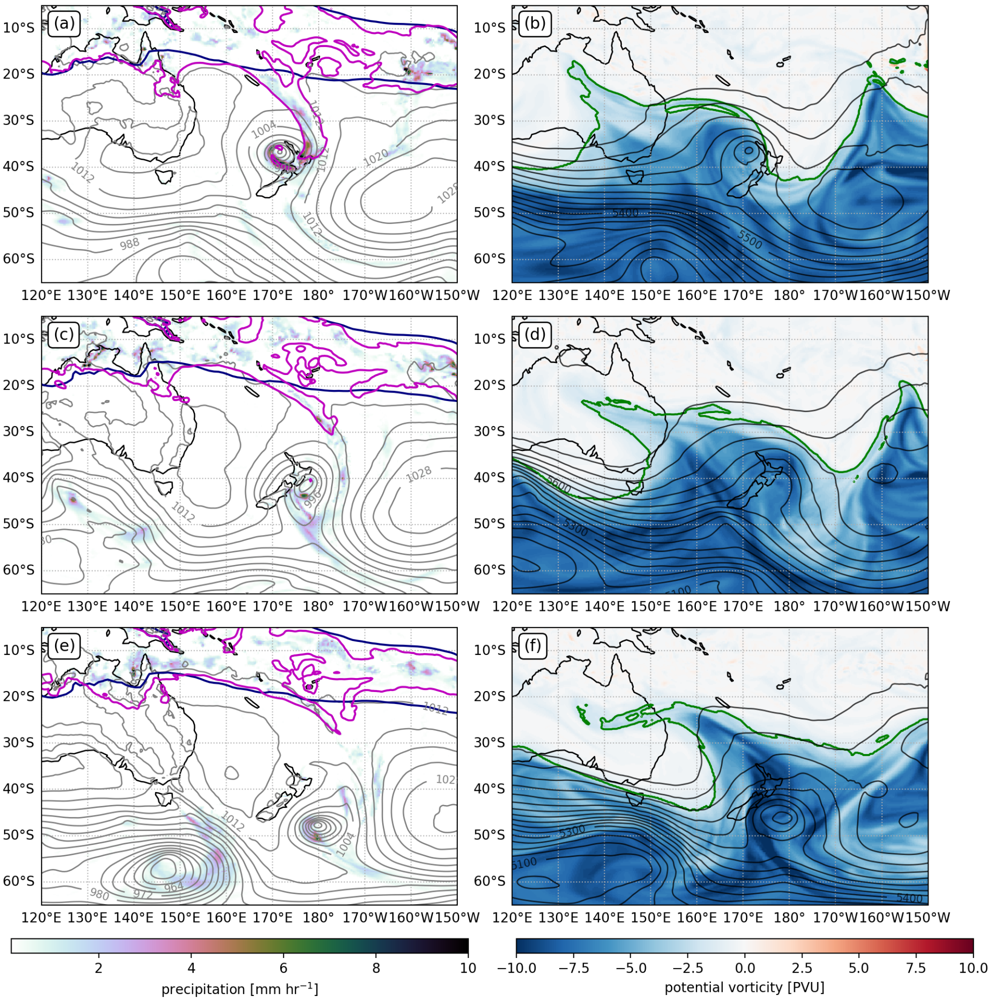

Figure 3. As in Figure 2 but for 12Z 04 January (a-b), 12Z 05 January (c-d), and 12Z 06 January (e-f).

Zealand, and the ridge generated by the interaction extends toward the southeast of the domain. Here, Rossby wave breaking causes PV mixing that ultimately results in local wave decay (McIntyre and Palmer, 1983). Following this, the cyclone weakens
155 as it slowly moves eastward over the South Pacific (not shown), indicating the end of the event.

The synoptic charts suggest that the extratropical interaction with the moist margin occurred on 03 January, resulting in rapid cyclogenesis and upper-level ridging. To gain further insight into the structure of the atmosphere at this time, we present zonal and meridional cross-sections (Figure 4) through the interaction along the red lines in Figure 2 e-f.

The zonal cross-section displays a prominent upper-level cyclonic PV anomaly to the west and an anticyclonic anomaly
160 to the east (Figure 4a). The dynamical tropopause extends down to around 400 hPa at 160E, indicating a deep cyclonic PV anomaly, while the anticyclonic PV anomaly is represented by a raised dynamical tropopause toward 100 hPa. There is also

https://doi.org/10.5194/egusphere-2026-3451
Preprint. Discussion started: 29 June 2026

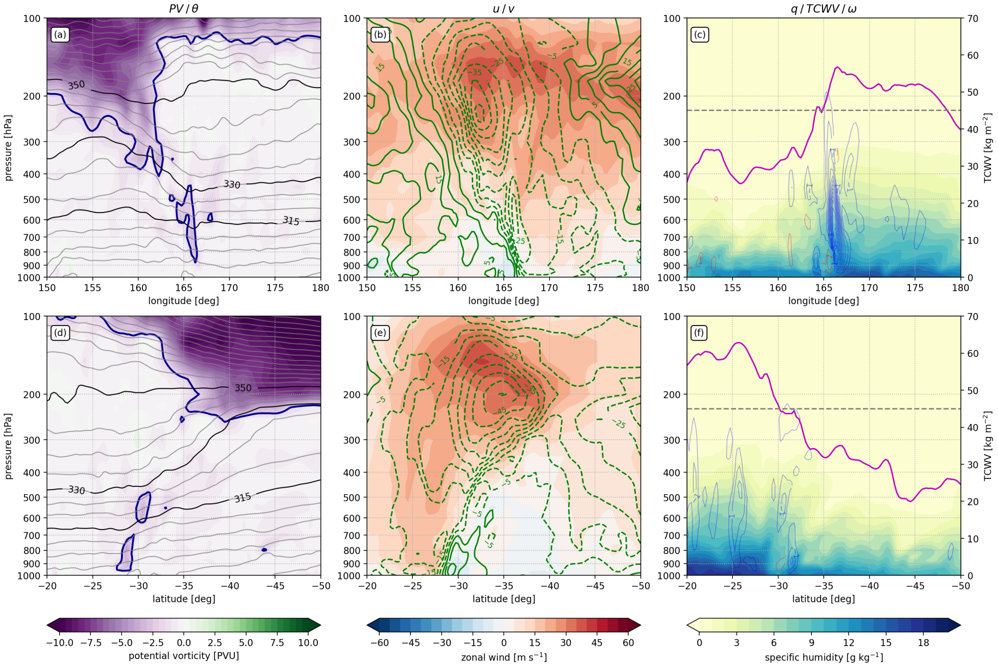

Figure 4. Zonal (a-c) and meridional (d-f) cross-sections through the centre of the low-pressure system on 12Z 03 January 2018, marked by red lines on Figure 2. Plotted are (a, d) potential vorticity in shading and potential temperature in contours with the dynamical tropopause in blue (2 PVU); (b, e) zonal wind in shading and meridional wind in contours every 2 m s^{-1} (negative values are dashed); and (c, f) specific humidity in shading, total column water vapour as the purple line with the moist margin threshold of 45 kg m^{-2} as the horizontal dashed grey line, and vertical motion in contours every 0.5 Pa s^{-1} (ascent is blue and descent is red).

some low-level cyclonic PV at around 165E that is presumably diabatically generated and related to the development of the surface low. The overall PV structure tilts westward with height, consistent with baroclinic intensification (Chang, 1993). This tilt is also reflected in the meridional winds (Figure 4b), which are northerly to the east and southerly to the west of the upper-level cyclone. The TCWV shows the moist margin situated around 165E with dry air to the west and moist air to the east (Figure 4c). There is strong localised ascent on the moist side, which also represents a transition between a shallow moist layer (up to around 800 hPa) and a deep moist layer (up to around 500 hPa). This ascending air is also poleward-moving, resembling a warm conveyor belt. The overall structure of the cross-sections is similar to the composite analysis, although significantly more detail is visible here.

The meridional cross-sections confirm the expected structure of the event (Figure 4 d-f). Low-level cyclonic PV is present around 30S, upper-level winds are largely poleward, and moisture decreases from the equator to the pole. Furthermore, the subtropical jet and moist margin are located at similar latitudes of approximately 30-35S, demonstrating an interaction between the two.

3.2 Moisture budget

We now examine a moisture budget to examine the processes leading to movement in the moist margin in this case study. For the sake of conciseness, we only present a single time at 12Z 03 Jan, which represents the strongest interaction between the moist margin and the extratropics. Similar conclusions exist throughout different times of the event. Maps of the budget terms are presented in Figure 5, along with a time series of budget terms averaged over the red box. Budget terms in the time series have been smoothed with a 24-hour moving average, as this can reduce noise and improve budget closure (Morris et al., 2025).

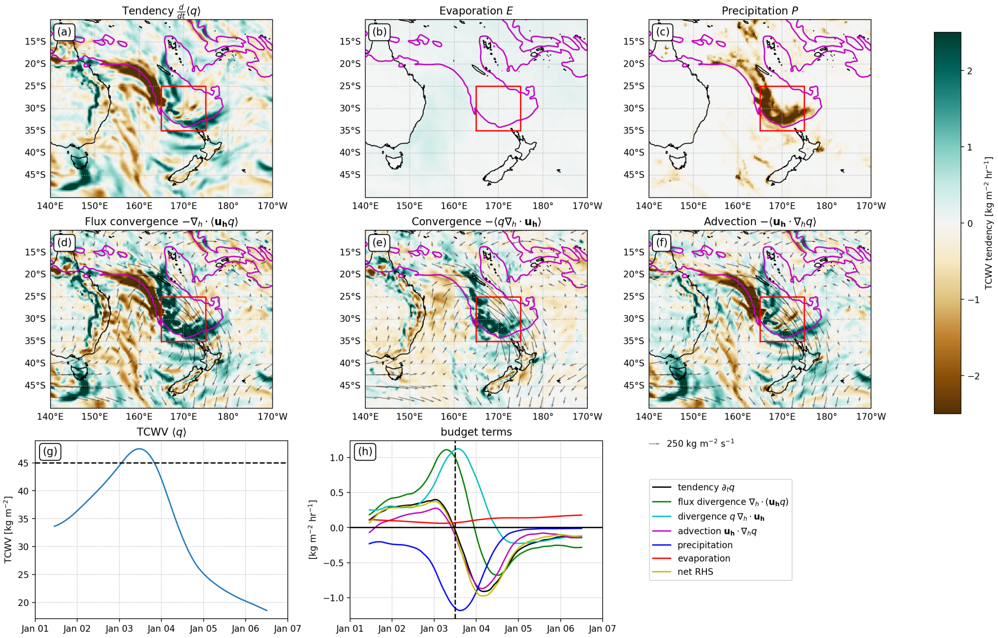

Figure 5. Moisture budget terms at 12Z 03 January for the case study. Panels g and h show the time series of terms averaged over the red box, which have been smoothed by a 24-hour moving average. The integrated vapour transport has been overlaid on panels d-f.

The moisture tendency displays clear moistening at the poleward edge of the moist margin perturbation (30-35S, 170-175E), meaning the margin is moving poleward (Fig. 5a). Meanwhile, strong drying exists to the northwest along the moist margin, indicating a dry intrusion that extends equatorward on the western flank of the cyclone. This dry intrusion does not result in a dry perturbation in the moist margin, but rather, returns the margin to its climatological position.

The evaporation term is small overall, but slightly enhanced along the shores of eastern Australia outside the moist margin (Fig. 5b), consistent with enhanced evaporation into cold, dry air, particularly in dry intrusions (Givon et al., 2024). The precipitation is heavy within the moist margin perturbation, with widespread areas receiving rates over 2.5 mm hr^{-1} (Fig. 5c).

The moisture flux convergence term (Fig. 5d) is also noisy, but overall matches the tendency fairly well. This pattern includes moistening at the poleward edge of the moist margin perturbation and drying to the northwest of the perturbation. The convergence is strong in highly precipitating areas. Aside from this, the flow within and outside the moist margin is generally

https://doi.org/10.5194/egusphere-2026-3451
Preprint. Discussion started: 29 June 2026

convergent and divergent, respectively. The pattern for moisture advection (Fig. 5e) is remarkably similar to that of the moisture tendency, even on finer scales. In this case, the poleward movement of the moist margin towards New Zealand and the equatorward movement in the Coral Sea is associated with the horizontal advection of water vapour.

The time series indicates that the area over the red box moistens until 03 January, after which it rapidly dries (Fig. 5g). The time series of budget terms reveals a balance between moistening through convergence and drying through precipitation, and the total moisture tendency closely matches the advection. The budget also closes very well with minimal difference between the total tendency and the sum of budget terms.

3.3 Trajectory analysis

To complement the moisture budget analysis, we also run back-trajectories using LAGRANTO for three key areas throughout the event (Fig. 6. These are:

1. The area inside the moist margin perturbation at 12Z 03 January (165-175E, 25-35S)
2. The same location two days later at 12Z 05 January, indicative of a dry intrusion following the event (165-175E, 25-35S)
3. The upper-level ridge also at 12Z 05 January (175-165W, 45-55S)

For area 1 (moist margin perturbation), we impose an additional constraint that the TCWV must be above 45 kg m^{-2} to ensure that we consider air only inside the moist margin. For areas 1 and 2, trajectories are launched from 700 hPa, where humidity anomalies are largest in moist margin perturbations (Robinson et al., 2024). For area 3 (upper-level ridge), trajectories are instead launched from 250 hPa. The horizontal spacing for trajectories is 0.5°, and they are evaluated every hour with full-resolution ERA5 data.

For the moist margin perturbation (6, left panels), there are two or three clear origins of air. The first and most common pathway is air from the deep tropics (north of 20S) that rises from low levels to 700 hPa. Another pathway is evident from the west, with some of these trajectories descending. These appear to be air parcels that move toward the southern boundary of the moist margin and are likely drier. Furthermore, another branch is apparent, originating from the northwest and remaining relatively constant with height, with these parcels finishing near the eastern region. The large number of parcels coming from the northwest is consistent with the approaching upper-level PV anomaly, which acts to draw moisture from the deep tropics poleward and eastward.

The distribution of traced variables for the moist margin perturbation is bimodal at early lead times, reflecting the split in trajectories. The pathway from the tropics comprises most of the moist air with specific humidity above 7.5 g kg^{-1}, pressure levels below 750 hPa, and likely high relative humidity. In contrast, the pathway from the west comprises drier air with specific humidity below 5 g kg^{-1} and pressure levels above 750 hPa. On average, air parcels rise and are heated in the final 24 hours, particularly those originating in the tropics. There is also a slight drying on average, although air parcels from the west appear to moisten in the final 48 hours. Both relative humidity and TCWV rise steadily in the final 72 hours.

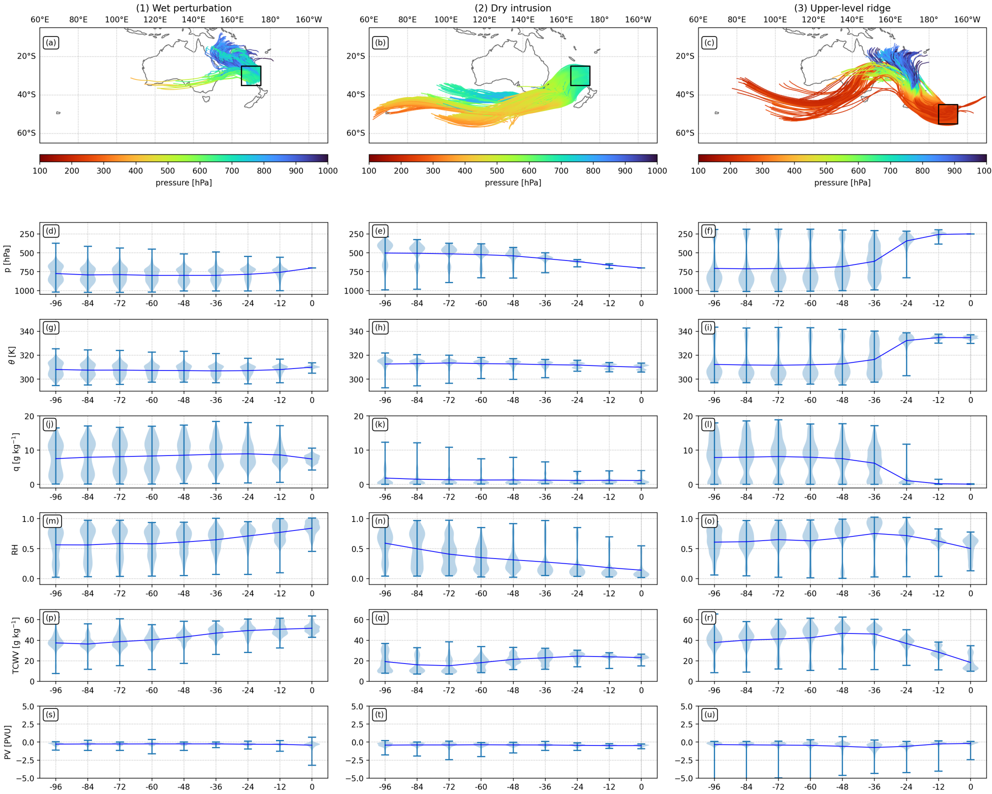

Figure 6. Trajectory analysis for three key areas during the case study as marked by [colour] boxes in Figures 2 and 3. Bottom panels show violin plots of traced specific humidity, potential temperature, and relative humidity, with the solid blue line denoting the mean of the distribution.

Two days later, there is a dramatic shift in the trajectories launched from the same region due to the progression of the interaction and cyclone (Figure 6, middle panels). All trajectories originate in the southwest, and the majority are descending, consistent with a dry intrusion following the event. There are slight differences in the trajectory pathways, with some parcels originating at lower levels and further north, travelling nearly horizontally. The traced variables indicate a steady descent on average from above 500 hPa to 700 hPa and slight cooling. The specific humidity remains low throughout. Interestingly, the relative humidity of air parcels decreases in time (likely due to adiabatic warming through descent while specific humidity remains unchanged); however, the TCWV increases slightly or remains near-constant.

Trajectories for the upper-level ridge (Figure 6, right panels) show two clearly distinct pathways. The first travels along the jet stream, remaining at pressure levels around 250 hPa. This air is dry with low specific humidity and potential temperature of around 330-340 K. However, the majority of air parcels originate from low levels in the tropics, similar to parcels inside the moist margin perturbation. These air parcels are moist with specific humidity values of 5-20 g kg^{-1} and potential temperatures of around 300-320 K. During the period -48 to -24 hours, these air parcels are rapidly heated and dried as they ascend within the warm conveyor belt of the cyclone. In the final 36 hours, there is also a drop in relative humidity and TCWV, likely due to the formation of precipitation. Also notable is that the majority of parcels at -48 hours have TCWV above 45 kg m^{-2}, meaning they are situated within the moist margin. By -12 hours, all of these trajectories now lie outside the moist margin. The PV also shows a slight tendency to more negative values (more cyclonic) around -36 hours before reverting to small negative values (more anticyclonic). This pattern may reflect diabatic heating along trajectories, with low-level parcels experiencing cyclonic PV tendencies and high-level parcels experiencing anticyclonic PV tendencies due to diabatically generated PV. However, the overall low PV magnitude (below 2 PVU) suggests the air within the upper-level ridge is tropospheric in origin. Note that some trajectories fall between these two categories, originating over eastern Australia in the mid-levels and ascending more slowly to 200 hPa.

Overall, these trajectories clearly demonstrate the tropical-extratropical interaction with the upper-level anticyclone intimately linked to ascent and diabatic heating, consistent with previous studies (e.g., Steinfeld et al., 2020; Hauser et al., 2023). Repeating the analysis at a different pressure level alters the proportion of air parcels between the two branches. Parcels initialised lower in the atmosphere tend to be more connected to the lower tropical branch, while parcels at higher levels tend to be more connected to the upper branch along the jet (not shown).

4 Latent heating experiments

4.1 Evolution and the cyclone and downstream flow

Figure 7 shows the cyclone tracks and central pressures of the ACCESS-rAM3 experiments compared to ERA5. The control run simulates the tracks and intensity of the observed cyclone well, with some minor differences after crossing New Zealand. The tracks for all latent heating experiments are also similar, moving south-eastward. However, the low-pressure system in the 0.5L experiment fails to intensify, moves more slowly, and disappears after the early hours of 06 January. Experiments with increased L exhibit a more meridionally-oriented track, beginning northward and ending poleward of the observed track, while experiments with reduced L exhibit a more zonally-oriented track.

The cyclone intensity is similar between experiments until around 12Z 03 January, which marks the peak of the interaction. From here on, the intensities diverge, with intensity increasing with latent heating. Note that the maximum cyclone intensity is monotonic with increasing L, although this occurs at slightly different times. Overall, these results suggest a significant dependence of cyclone intensity on latent heating during the tropical-extratropical interaction.

We now further examine the synoptic structure during the peak of the extratropical interaction with the moist margin (12Z 03 January). The results are shown in Figure 8. Comparison with ERA5 data in Figure 2e-f suggests that the control simulation captures the overall structure of the event well, with similar patterns in MSLP, PV, TCWV and geopotential height. For conciseness, results from the 0.75L and 1.25L experiments are omitted; however, a monotonic progression from 0.5L to 1.5L is evident in the synoptic structure. The low-pressure system in the control experiment is located east of Australia at around 165E and 27S. The low in the 0.5L experiment is further southwest, closer to 160E, 30S. All experiments show prominent rainfall to the north and east of the cyclone, perhaps marking the cold and warm fronts, respectively, although the orientation slightly

https://doi.org/10.5194/egusphere-2026-3451
Preprint. Discussion started: 29 June 2026

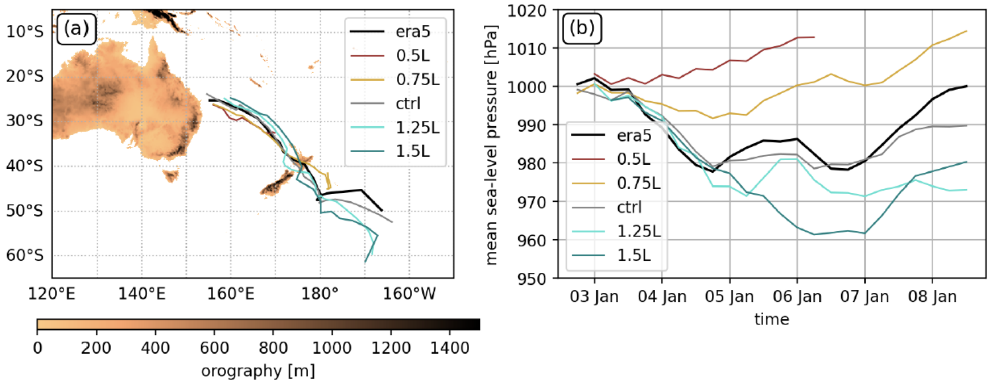

Figure 7. (a) ACCESS-rAM3 domain for the 2018 subtropical cyclone case study. The orography is shaded. The cyclone tracks are overlaid in panel (a). Panel (b) shows a time series for the minimum sea level pressure of the cyclone for the five experiments.

differs between experiments. In the 1.5L experiment, precipitation is concentrated in a single line from northwest to southeast and extends into the deep tropics to around 15S. Overall, precipitation increases with increasing latent heating, including but not limited to the region around the cyclone.

Panels d-f of Figure 8 show a prominent moist margin perturbation around New Zealand co-located with an upper-level ridge, consistent with ERA5. However, this is somewhat different in the 0.5L experiment, which shows a moist margin perturbation further west as well as a weaker upper-level ridge. The upper-level cyclone to the west is similar for all experiments; however, the upper-level cyclone to the east is notably weaker in the 0.5L experiment. Also note that the moist margin is generally located further poleward with decreased latent heating, consistent with a domain-mean increase in TCWV, which will be elaborated on later. The dynamical tropopause (green line) is also generally located further poleward with increasing latent heating.

The difference between the experiments becomes more apparent two days later, on 12Z 05 January, as shown in Figure 9. For the control and 1.5L experiments, the cyclone is strong and situated southeast of New Zealand, consistent with ERA5, with an associated frontal band to the east extending into the tropics. In the 0.5L experiment, the low is weak and still situated northwest of New Zealand, although the locations of the flanking high-pressure systems are similar. The moist margin perturbation is still present, but located further east. In the control simulation, the moist margin position is close to ERA5. In the 0.5L experiment, it extends further poleward toward New Zealand and then eastward. The more poleward moist margin in 0.5L may be due to reduced precipitation leading to less local drying. For the 1.5L experiment, the moist margin perturbation still extends well poleward but is more meridionally oriented, connecting to the tropical well around the dateline. This structure is associated with strong precipitation near 180E, 30S.

The difference in the upper-level ridge is also more apparent between experiments. Notably, the dynamical tropopause in the 1.5L experiment is strongly displaced poleward towards 60S, with overturning contours indicating prominent cyclonic Rossby wave breaking. In the control simulation, the dynamical tropopause extends to only 35-40S, but a clear anticyclonic

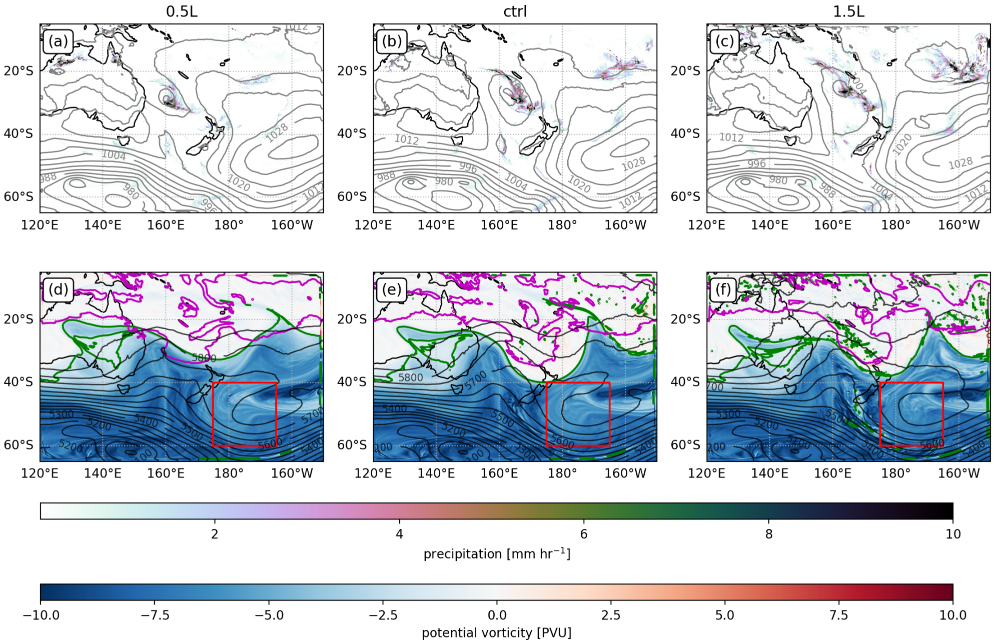

Figure 8. Synoptic plots of the case study for 12Z 03 January 2018 for 0.5L (a, d), control (b, e), and 1.5L (c, f) simulations. Panels a-c display mean sea level pressure in contours every 4 hPa and precipitation rates in shading. Panels d-f display the moist margin at TCWV=45 kg m^{-2}, 500 hPa geopotential height every 50 m in black contours, 350 K potential vorticity in shading, and the dynamical tropopause defined by -2 PVU in the green line. The red box indicates the area of analysis for the potential vorticity budget.

PV anomaly is present east of New Zealand. In the 0.5L experiment, there is no anticyclonic PV anomaly present in the area, indicating a weakened tropical-extratropical interaction.

Overall, these results suggest that the strength of the extratropical interaction with the moist margin is strongly moderated by latent heating. Not only does the cyclone strength increase, but the accompanying upper-level ridge also strengthens as latent heating increases. The interaction is also evident through the coupling of the moist margin and dynamical tropopause contours in the bottom rows of Figures 8 and 9. In the control and 1.5L experiments, these contours often follow somewhat in parallel. However, in the 0.5L experiment, these contours do not appear to be related, indicating decoupling between PV and the moist margin. This result is most evident in Figure 9e, where the moist margin perturbation exists in the absence of any meaningful PV structure

4.2 Potential vorticity budget

The PV budget is evaluated over a key region of upper-level ridging during the interaction on 03 January, as marked by the red boxes on Figures 8. For simplicity, this region is fixed in time. An extension of this work could be to evaluate PV budgets with a domain that follows the ridge or PV objects, for example, as in Teubler and Riemer (2016). As with the moisture budget,

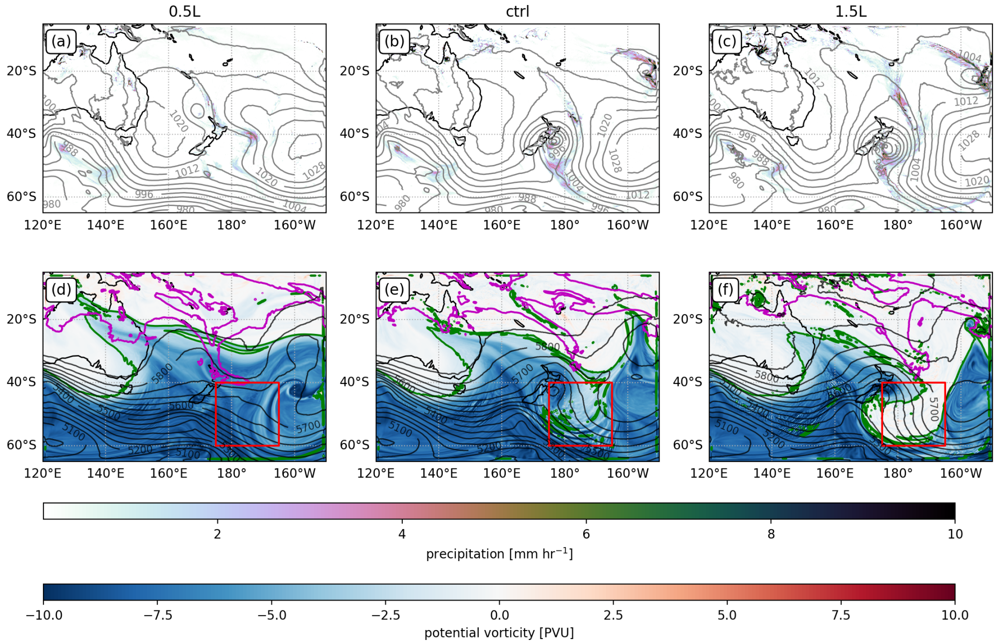

Figure 9. As in Figure 8 but for 12Z 05 January 2018.

budget terms are further smoothed with a 24-hour moving average to reduce noise. Similar analysis is performed on 05 January when the ridge moves poleward, but results are broadly consistent with those on 03 January, so only the former is presented here.

The budget results are presented in Figure 10. The left panels show synoptic maps of the PV and PV budget terms at 12Z 03 January 2018, while the right panels show time series of values averaged over the red box. For the following discussion, recall that cyclonic PV is negative in the Southern Hemisphere.

The average PV inside the red box is shown in Figure 10b. All experiments show a tendency toward ridging (low-magnitude PV) peaking around 12Z 03 January, consistent with the structure seen in the control experiment in panel a. However, the extent of the ridging varies strongly by experiment, with the control, 1.25L and 1.5L experiments having similar strength, and the 0.5L and 0.75L experiments substantially weaker. The strength of the ridging gradually decreases over the coming days as the system propagates eastward. A similar evolution can be seen in the PV anomalies (panel d), although the difference is reduced, reflecting changes in the background PV between the different experiments.

The maps of PV advection by the rotational (panel e) and divergent (panel g) winds show clear PV tendencies around the ridge. Rotational winds tend to follow along the ridges and troughs, contributing to ridging and troughing at the east and west boundaries of the ridge, respectively. This pattern is consistent with eastward propagation through the mean westerly flow. The divergent winds indicate upper-level divergence centred around 168E, 32S. These winds interact with the dynamical tropopause to the southwest, contributing to anomalous ridging on the rear flank of the upper-level anticyclone. However, divergent winds

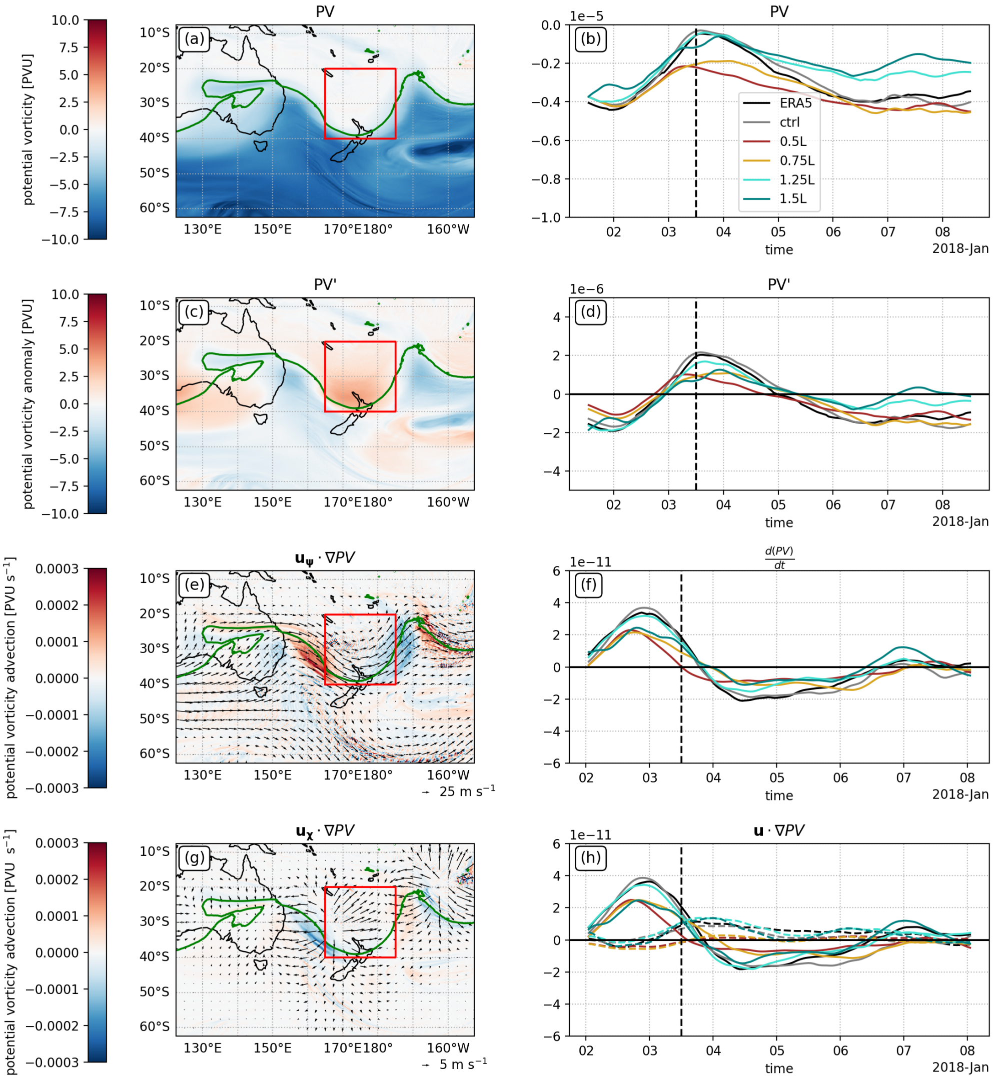

Figure 10. 350 K potential vorticity budget for Region A 165-185E, 20-40S for ERA5 and the five ACCESS-rAM3 experiments. The left column shows values of PV (a), PV anomaly (c), PV advection by the rotational wind (e), and PV advection by the divergent wind (g) at 12Z 03 January 2018 in the control simulation. The scale for the divergent winds is exaggerated by a factor of 5 compared to the rotational winds. The right column shows time series of (b) average PV within region A, (d) average PV anomaly, (f) PV tendency, and (h) total PV advection (solid lines) and advection by the divergent part of the wind (dashed lines). The time of interest 12Z 03 January 2018 is marked by the vertical dashed black line.

contribute little along the eastern flank of the anticyclone. Note that the patterns for rotational and divergent PV advection are similar but of opposite sign. This may indicate that the divergent winds act to slow down the propagation of the PV anomalies,

https://doi.org/10.5194/egusphere-2026-3451
Preprint. Discussion started: 29 June 2026

as well as contributing to the growth of the ridge, and may lead to atmospheric blocking (Steinfeld et al., 2020; Hauser et al., 2023).

The average PV tendency over the red box is shown in Figure 10f, and shows a strong anticyclonic tendency over 02-03 January, followed by weaker cyclonic tendencies until 07 January. This pattern closely matches the PV advection in panel h, consistent with minimal direct modification of PV on the 350 K isentrope. The contribution of the divergent part of the wind to PV tendencies is shown in the dashed lines. Generally, this is positive throughout the event for control, 1.25 and 1.5L experiments. The contribution of the divergent winds is largest around 04 January, when the PV tendency becomes cyclonic. This represents the approach of the following trough from the west. The PV advection by divergent winds is substantially smaller in the 0.5L and 0.75L experiments, and not substantially increased in the 1.25L and 1.5L experiments, perhaps indicative of nonlinearities or threshold-like behaviour leading to the presence or absence of convection.

4.3 Other changes due to latent heating modification

The results of the above experiments indicate that changes to the latent heating constants L have a noticeable effect on the overall structure of the atmosphere, for example, through changes in the mean position of the moist margin and dynamical tropopause. This result is not unexpected, given that the experiments fundamentally change the way the atmosphere works. We now examine these changes in further detail.

Figure 11 presents the effects of scaled latent heating constants on the time- and domain-mean structure of the atmosphere. In panel a, we plot terms for the vertically integrated moisture budget as a function of the latent heating scaling factor L_{fact}. The results reveal a clear increase in total precipitation as L_{fact} increases. Notably, this increase almost exclusively comes from the convective precipitation, with little change in large-scale (resolved) precipitation. The mean evaporation rate also increases slightly with L_{fact}, although to a lesser extent. This result is perhaps surprising, given that one may expect evaporation to decrease due to the increased energy required to evaporate water. Analysis of a simple bulk-flux formula demonstrates that this is explained by decreased near-surface humidity and increased wind speed (not shown). Also note that sea surface temperatures are prescribed in this experiment, meaning evaporation and latent heat fluxes do not feed back on the ocean, as would happen in the real world. Overall, there is a slight decrease in the average TCWV with increasing latent heating from around 29.5 to 27.5 kg m^{-2}. This decrease is consistent with precipitation increases (drying) exceeding decreases in evaporation (moistening).

The domain-mean change in TCWV may have implications for the moist margin, in particular, the suitable TCWV threshold in the model. The moist margin threshold is typically defined as the antimode of the global tropical TCWV distribution, which cannot be evaluated in a short regional model simulation. Therefore, we opt for the simple choice of keeping 45 kg m^{-2} as the moist margin threshold for ERA5 and all model experiments.

Figure 11b shows how changes to L_{fact} affect the vertical thermal structure of the atmosphere through profiles of potential temperature relative to the control simulation. Simulations with $L_{fact} > 1$ are marginally cooler at low levels (below 850 hPa) and substantially warmer at upper levels (above 850 hPa), with a maximum difference around 200-300 hPa. The warming in the upper levels is consistent with greater heat release from convection, while the cooling in lower levels may be due to enhanced

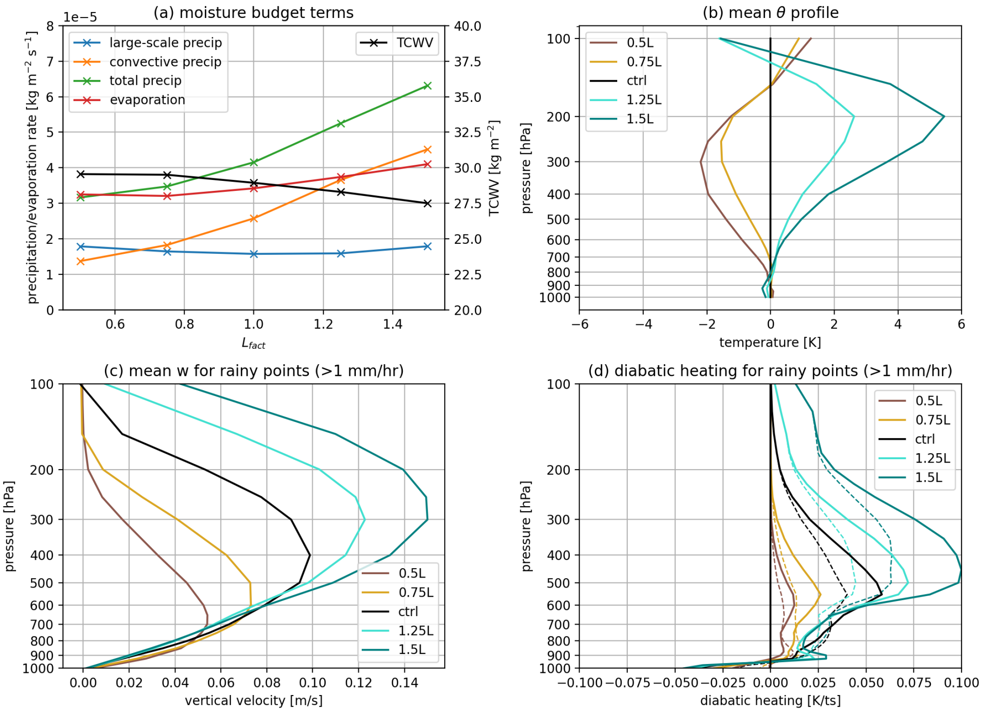

Figure 11. Effect of varying latent heating constants for time- and domain-mean moisture budget terms (a), potential temperature profiles compared to the control simulation, vertical motion profiles for rainy points, defined as rates with > 1 mm hr^{-1} (c), and diabatic heating profiles (d), where total heating is denoted by solid lines and the contribution from the convection scheme is denoted by dashed lines.

evaporative cooling from the surface or evaporation of rainwater. Note that a change in lapse rate does not necessarily imply a change in stability, since moist adiabats will differ with modified values of L_{fact}.

The mean vertical velocity profiles for rainy grid points (defined as precipitation rates greater than 1 mm hr-1) are presented in Figure 11c. There is an increase in both the upward vertical velocity and the height of its maximum with increasing L_{fact}. Latent heating is the key process that drives conditional instability in the atmosphere, since the heating of air parcels through condensation makes them more positively buoyant. Increasing L_{fact} is therefore expected to increase the intensity and depth of acceleration of updraughts, leading to stronger and more top-heavy convection. This reasoning is consistent with the results here.

Figure 11d shows the vertical profiles of diabatic heating (temperature adjustments) over the same rainy points. All experiments show heating in the mid- to upper-troposphere, and cooling near the surface below 950 hPa. The magnitude of the heating and cooling monotonically increases with the latent heating. Similarly to the vertical velocity profiles, the height of maximum heating increases from 600 hPa in the 0.5L experiment to 450 hPa in the 1.5L experiment, although this increase is smaller than that of the vertical velocity. About two-thirds of the diabatic heating in the profile is produced by the convection scheme, with the remainder coming from large-scale (i.e., resolved) cloud and precipitation processes, and little contribution

https://doi.org/10.5194/egusphere-2026-3451
Preprint. Discussion started: 29 June 2026

from other physical processes, including radiation (not shown). At lower levels (below around 700 hPa), the total heating is less than the convective heating, suggesting that large-scale cloud processes contribute to diabatic cooling, likely through evaporative cooling of rainwater (e.g., Maybee et al., 2025).

5 Discussion and conclusions

We have presented a case study of a clear extratropical interaction with the tropical moist margin. The interaction occured alongside rapid cyclogenesis in the Tasman Sea that led to gale-force winds and flooding over New Zealand (Insurance Council of New Zealand, 2018). The case study displays a clear ordering of events as follows:

1. Before the interaction, the moist margin was already located poleward of its typical position over north-eastern Australia and the Coral Sea (01 January) due to a previous interaction between a tropical cyclone and cold front.
2. A deep cyclonic PV anomaly approaches the moist margin from the southwest (02 January).
3. When this cyclonic anomaly is close enough to the moist margin, the interaction occurs. This results in a large poleward displacement of the moist margin through horizontal moisture advection, with air parcels travelling poleward from the deep tropics (03 January).
4. The interaction results in rapid cyclogenesis and intensification of an upper-level ridge to the east of the cyclone from rapid ascent and heating in the cyclone's warm conveyor belt (04 January).
5. The moist margin returns to its usual position as cold and dry air behind the cyclone spreads into the tropics, but the cyclone continues to develop as it moves poleward, with further amplification of the ridge and downstream development evident (05-06 January).

5.1 Processes linking the moist margin with the extratropics

Based on the results of this case study, a schematic of the processes involved during extratropical interactions with the moist margin is depicted in Figure 12. The diagram resembles the case study on 03 January, which could be considered the peak of the interaction for this event (Figure 2e-f). The interaction occurs in two directions as follows:

- When a cyclonic PV anomaly approaches the moist margin, poleward flow at low- to mid-levels along its eastern flank advects water vapour poleward, leading the moist margin to shift poleward.
- When the moist margin is perturbed far poleward, enhanced convection and upper-level divergence during the interaction amplify the upper-level ridge and may lead to downstream development.

Other significant factors labelled in Figure 12 include the low-level circulation, which may result from the vertical extension of the upper-level cyclonic PV anomaly, and the diabatic heating within the convective region. Results from the ACCESS-rAM3 experiments suggest that the strength of the interaction is strongly related to diabatic heating through its effects on the

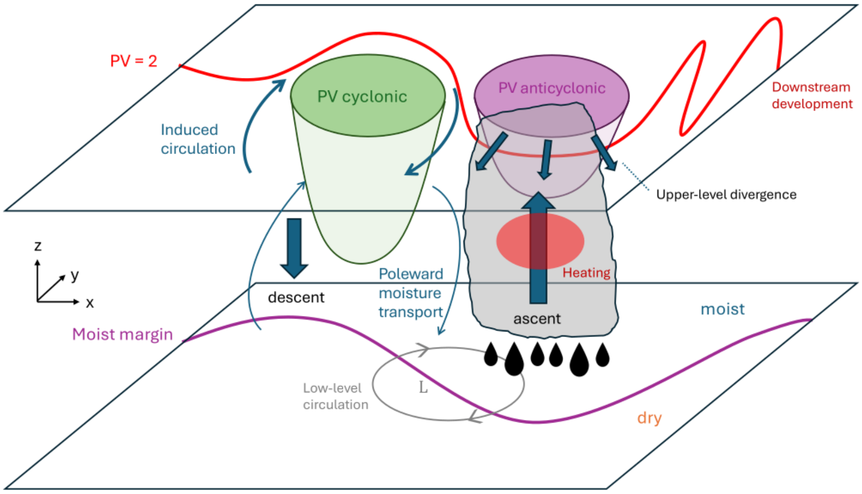

Figure 12. Proposed schematic for interactions between extratropical potential vorticity anomalies and the moist margin in the Southern Hemisphere.

upper-level divergence. These results are consistent with a broad body of research highlighting the role of diabatic heating in extratropical dynamics (Wernli and Gray, 2024, and references therein) and tropical-extratropical interactions (Knippertz, 2007; Stan et al., 2017). In this case, the interaction amplifies the wave packet to the point that it results in Rossby wave breaking. A recent study by Barnes et al. (2025) proposes that cyclonic Rossby wave breaking may be wave-generative, which appears consistent with this case study.

The structure of extratropical interactions with the moist margin, along with the importance of diabatic heating, is reminiscent of moist baroclinic instability. Here, condensational heating further enhances a baroclinic wave (Mak, 1982). Moist baroclinic instability is particularly relevant to explosive cyclogenesis (Reed and Albright, 1986; Mak, 1994; Zou et al., 2025). Another related phenomenon is the diabatic Rossby wave, for which the advection of warm and moist air along the eastern flank of a low-level vortex results in upward motion, heating, and the diabatic generation of PV, maintaining the vortex in the direction of the thermal wind (Raymond and Jiang, 1990; Parker and Thorpe, 1995; Moore and Montgomery, 2004; Boettcher and Wernli, 2011). Diabatic Rossby waves bear many similarities to the processes studied in moist margin interactions, except that in the present study, we focus on meridional advection of moisture rather than heat. The relationship between diabatic Rossby waves and the moist margin could be the topic of future work.

The key process binding PV anomalies and the moist margin together appears to be deep moist convection, which must be strong and located close enough to the upper-level jet to have a significant impact. Notably, the moist margin itself does not appear to directly affect extratropical PV, for example, as seen in the ACCESS-rAM3 experiments, where reducing latent heating constants results in a more poleward margin but no substantial interaction. We therefore surmise that the role of the moist margin perturbation is to permit heavy convection, with the associated condensational heating interacting with the extratropics if it occurs close to strong upper-level PV gradients (i.e., the jet stream).

An outstanding question is how well the results of this case study would generalise. Robinson (2026, Chapter 5) demonstrates that the moist margin is strongly perturbed and heavy precipitation is produced when a cyclonic PV anomaly approaches the moist margin, but only when the cyclonic PV anomaly extends into the lower troposphere, as is evident in the cross-sections for this study (Figure 4). Therefore, the depth of the PV anomaly is an important predictor for the strength of the interaction. Deep cyclonic PV anomalies (stratospheric intrusions) are known to have a stronger connection with the low levels, for example, through cyclogenesis and generation of cutoff lows (Barnes et al., 2021a, b).

Another challenge is that the direction of influence between PV anomalies and the moist margin is difficult to establish. Although we propose that the PV structure influences the moist margin first and then feeds back onto the PV, our results demonstrate that the development of the moist margin and PV anomalies is near-concurrent. Alternatively, it is possible that a succession of cyclonic PV anomalies may combine to enhance moisture transport and deformation of the moist margin, similar to results found for tropical plumes over Africa (Knippertz, 2007).

5.2 Future research directions

We now outline some opportunities for further research which could lend additional insight into the mechanisms of extratropical interactions with the tropical moist margin:

- The influence of the upper-level cyclonic PV anomaly on the moist margin could be clarified with a piecewise PV inversion technique (Davis, 1992). Here, the low- to mid-level flow and associated moisture advection could be attributed to the cyclonic PV anomaly. PV inversion may be feasible for a case study, but it will likely prove challenging in a climatological study due to its complexity and its reduced applicability in lower latitude regions.

- Further consideration could be made into the role of persistent or successive upper-level cyclonic PV anomalies on the moist margin. Informal analysis of weather charts reveals a common pattern of moisture cycling into and out of the tropics though interactions with the extratropics, and it is highly plausible that such a combination of events would result in a strongly deformed moist margin and severe rainfall (Knippertz and Martin, 2005).

- Further model experiments should be carried out. Experiments could include additional case studies, sensitivity testing, or ensemble analysis to determine how well the results generalise. Alternatively, the model could be run over a larger area for a longer period to include multiple events and/or further examine how modified latent heating affects the general structure of the atmosphere. Another option is to run the model at a higher resolution (i.e. storm-resolving) to examine how the representation of convection affects the interaction, noting that most heating in the current setup is generated by the convection scheme. In particular, it has been shown that the Unified Model at kilometre-scale with convection-permitting settings produces a much more accurate representation of the moist margin than settings with a convective parameterisation (Bassford et al., 2025). Finally, it would be interesting to compare the L-modification approach used here with an approach that modifies temperature adjustments, as in previous studies (Büeler and Pfahl, 2017; Steinfeld et al., 2020; Zou et al., 2025).

- Idealised modelling could provide further insight into the mechanisms controlling extratropical interactions with the moist margin. Here, we could modify one factor of the interaction while keeping others constant, or examine the response to imposed idealised heating or vorticity anomalies. Interactions could be investigated across the hierarchy of model complexities, for example, through mechanism-denial experiments to target the importance of a specific process (Maher et al., 2019).
- The trajectory analysis could be enhanced by a moisture source diagnostic (Sodemann et al., 2008; Sodemann, 2025), which would provide information on the origins of water vapour in moist margin perturbations, as well as the potential for moisture recycling (Dominguez et al., 2006).

5.3 Conclusions

This study has examined the mechanisms controlling extratropical interactions with the moist margin through analysis of a case study in the Tasman Sea in January 2018. When a deep cyclonic PV anomaly approaches the moist margin, moisture is displaced poleward and eastward from the deep tropics into the subtropics through horizontal advection, moving the moist margin poleward. Upper-level divergence above the region of heavy precipitation within the perturbed moist margin contributes to ridge building and downstream development through the poleward advection of anticyclonic PV. Both the strength of the cyclone and the upper-level ridge strongly depend on the strength of latent heating, highlighting the importance of moist processes, especially the strength and location of convection, on the evolution of such events. These findings reinforce the need to develop models with accurate representations of moist processes to better understand and predict extreme precipitation in the subtropics.

Code and data availability. ERA5 and ERA5-Land reanalysis data are publicly available from the ECMWF Copernicus Climate Data Store (Hersbach et al., 2020; Muñoz-Sabater et al., 2021). The ACCESS-rAM3 model is available for researchers to run on the National Computational Infrastructure (NCI) in Australia (https://www.access-nri.org.au/models/access-ram/). The LAGRANTO (Sprenger and Wernli, 2015) and TempestExtremes (Ullrich et al., 2021) algorithms are publicly available on multiple platforms. The code used to generate the figures is available upon request.

Author contributions. CR performed the formal analysis and prepared the original manuscript with contributions from all coauthors. BW, CE and PG provided vital support in developing and running the ACCESS-rAM3 model. SN, BW and CJ gave important guidance and feedback throughout the project.

Competing interests. The authors declare that they have no conflict of interest.

Acknowledgements. This research was undertaken with the assistance of resources from the National Computational Infrastructure (NCI Australia), an NCRIS-enabled capability supported by the Australian Government. This research also used the ACCESS-NRI's model ACCESS-rAM3 infrastructure, which is enabled by the Australian Government's National Collaborative Research Infrastructure Strategy (NCRIS), and is based off a modelling framework provided by the Met Office. We also thank Emma Howard and Matthew Wheeler for providing useful comments on the paper draft.

References

Ayat, H., Lane, T. P., Wales, S., Reeder, M. J., and Huang, Y.: Rapid Surface Drying During the Black Summer Bushfires in Australia: Insights From High-Resolution Simulations, Journal of Geophysical Research: Atmospheres, 130, https://doi.org/10.1029/2024jd041706, 2025.

Barnes, M. A., Ndarana, T., and Landman, W. A.: Cut-off lows in the Southern Hemisphere and their extension to the surface, Climate Dynamics, 56, 3709–3732, https://doi.org/10.1007/s00382-021-05662-7, 2021a.

Barnes, M. A., Ndarana, T., Sprenger, M., and Landman, W. A.: Stratospheric intrusion depth and its effect on surface cyclogenesis: An idealized PV inversion experiment, Weather and Climate Discussions, p. 1–30, https://doi.org/10.5194/wcd-2021-24, 2021b.

Barnes, M. A., Reeder, M. J., and Ndarana, T.: Rossby Wave Breaking Morphologies on the Southern Hemisphere Dynamical Tropopause, Journal of Climate, 38, 4825–4844, https://doi.org/10.1175/jcli-d-24-0461.1, 2025.

Bassford, J., Marsham, J., Maybee, B., and Parker, D. J.: Kilometre-Scale Model with Explicit Convection Captures Global-Scale Bimodality of Total Column Water Vapour, Geophysical Research Letters, https://doi.org/10.22541/essoar.175130600.04060741/v1, 2025.

Best, M. J., Pryor, M., Clark, D. B., Rooney, G. G., Essery, R. L. H., Ménard, C. B., Edwards, J. M., Hendry, M. A., Porson, A., Gedney, N., Mercado, L. M., Sitch, S., Blyth, E., Boucher, O., Cox, P. M., Grimmond, C. S. B., and Harding, R. J.: The Joint UK Land Environment Simulator (JULES), model description – Part 1: Energy and water fluxes, Geoscientific Model Development, 4, 677–699, https://doi.org/10.5194/gmd-4-677-2011, 2011.

Boettcher, M. and Wernli, H.: Life Cycle Study of a Diabatic Rossby Wave as a Precursor to Rapid Cyclogenesis in the North Atlantic—Dynamics and Forecast Performance, Monthly Weather Review, 139, 1861–1878, https://doi.org/10.1175/2011mwr3504.1, 2011.

Brown, A., Milton, S., Cullen, M., Golding, B., Mitchell, J., and Shelly, A.: Unified Modeling and Prediction of Weather and Climate: A 25-Year Journey, Bulletin of the American Meteorological Society, 93, 1865–1877, https://doi.org/10.1175/bams-d-12-00018.1, 2012.

Büeler, D. and Pfahl, S.: Potential Vorticity Diagnostics to Quantify Effects of Latent Heating in Extratropical Cyclones. Part I: Methodology, Journal of the Atmospheric Sciences, 74, 3567–3590, https://doi.org/10.1175/jas-d-17-0041.1, 2017.

Chang, E. K. M.: Downstream Development of Baroclinic Waves As Inferred from Regression Analysis, Journal of the Atmospheric Sciences, 50, 2038–2053, 1993.

Clark, D. B., Mercado, L. M., Sitch, S., Jones, C. D., Gedney, N., Best, M. J., Pryor, M., Rooney, G. G., Essery, R. L. H., Blyth, E., Boucher, O., Harding, R. J., Huntingford, C., and Cox, P. M.: The Joint UK Land Environment Simulator (JULES), model description – Part 2: Carbon fluxes and vegetation dynamics, Geoscientific Model Development, 4, 701–722, https://doi.org/10.5194/gmd-4-701-2011, 2011.

Davis, C. A.: Piecewise Potential Vorticity Inversion, Journal of the Atmospheric Sciences, 49, 1397–1411, 1992.

Dominguez, F., Kumar, P., Liang, X., and Ting, M.: Impact of Atmospheric Moisture Storage on Precipitation Recycling, Journal of Climate, 19, 1513–1530, 2006.

Givon, Y., Keller, D., Pennel, R., Drobinski, P., and Raveh-Rubin, S.: Decomposing the role of dry intrusions for ocean evaporation during mistral, Quarterly Journal of the Royal Meteorological Society, 150, 1791–1808, https://doi.org/10.1002/qj.4670, 2024.

Hauser, S., Teubler, F., Riemer, M., Knippertz, P., and Grams, C. M.: Towards a holistic understanding of blocked regime dynamics through a combination of complementary diagnostic perspectives, Weather and Climate Dynamics, 4, 399–425, https://doi.org/10.5194/wcd-4-399-2023, 2023.

Hersbach, H., Bell, B., Berrisford, P., Hirahara, S., Horányi, A., Muñoz-Sabater, J., Nicolas, J., Peubey, C., Radu, R., Schepers, D., Simmons, A., Soci, C., Abdalla, S., Abellan, X., Balsamo, G., Bechtold, P., Biavati, G., Bidlot, J., Bonavita, M., Chiara, G., Dahlgren, P., Dee, D., Diamantakis, M., Dragani, R., Flemming, J., Forbes, R., Fuentes, M., Geer, A., Haimberger, L., Healy, S., Hogan, R. J., Hólm, E., Janisková, M., Keeley, S., Laloyaux, P., Lopez, P., Lupu, C., Radnoti, G., Rosnay, P., Rozum, I., Vamborg, F., Villaume, S., and Thépaut, J.: The ERA5 global reanalysis, Quarterly Journal of the Royal Meteorological Society, 146, 1999–2049, https://doi.org/10.1002/qj.3803, 2020.

Hoskins, B. J., McIntyre, M. E., and Robertson, A. W.: On the use and significance of isentropic potential vorticity maps, Quarterly Journal of the Royal Meteorological Society, 111, 877–946, 1985.

Insurance Council of New Zealand: Media Release, https://www.icnz.org.nz/industry/media-releases/first-storm-of-2018-costs-more-than-26m/, accessed: 2025-11-10, 2018.

Juckes, M. and Smith, R. K.: Convective destabilization by upper-level troughs, Quarterly Journal of the Royal Meteorological Society, 126, 111–123, https://doi.org/10.1002/qj.49712656206, 2006.

Keller, J. H., Grams, C. M., Riemer, M., Archambault, H. M., Bosart, L., Doyle, J. D., Evans, J. L., Galarneau, T. J., Griffin, K., Harr, P. A., Kitabatake, N., McTaggart-Cowan, R., Pantillon, F., Quinting, J. F., Reynolds, C. A., Ritchie, E. A., Torn, R. D., and Zhang, F.: The Extratropical Transition of Tropical Cyclones. Part II: Interaction with the Midlatitude Flow, Downstream Impacts, and Implications for Predictability, Monthly Weather Review, 147, 1077–1106, https://doi.org/10.1175/mwr-d-17-0329.1, 2019.

Knippertz, P.: Tropical–extratropical interactions related to upper-level troughs at low latitudes, Dynamics of Atmospheres and Oceans, 43, 36–62, https://doi.org/10.1016/j.dynatmoce.2006.06.003, 2007.

Knippertz, P. and Martin, J. E.: Tropical plumes and extreme precipitation in subtropical and tropical West Africa, Quarterly Journal of the Royal Meteorological Society: A journal of the atmospheric sciences, applied meteorology and physical oceanography, 131, 2337–2365, 2005.

Lynch, P.: Partitioning the Wind in a Limited Domain, Monthly Weather Review, 117, 1492–1500, 1989.

Maher, P., Gerber, E. P., Medeiros, B., Merlis, T. M., Sherwood, S., Sheshadri, A., Sobel, A. H., Vallis, G. K., Voigt, A., and Zurita-Gotor, P.: Model Hierarchies for Understanding Atmospheric Circulation, Reviews of Geophysics, 57, 250–280, https://doi.org/10.1029/2018rg000607, 2019.

Mak, M.: On Moist Quasi-Geostrophic Baroclinic Instability, Journal of the Atmospheric Sciences, 39, 2028–2037, 1982.

Mak, M.: Cyclogenesis in a conditionally unstable moist baroclinic atmosphere, Tellus A, 46, 14–33, https://doi.org/10.1034/j.1600-0870.1994.00003.x, 1994.

Mapes, B. E., Chung, E. S., Hannah, W. M., Masunaga, H., Wimmers, A. J., and Velden, C. S.: The Meandering Margin of the Meteorological Moist Tropics, Geophysical Research Letters, 45, 1177–1184, https://doi.org/10.1002/2017gl076440, 2018.

Maybee, B., Bassford, J., Marsham, J. H., Lewis, H., Field, P., Klein, C., and Parker, D. J.: How sensitive are Sahelian mesoscale convective systems to cold-pool suppression?, Quarterly Journal of the Royal Meteorological Society, https://doi.org/10.1002/qj.5032, 2025.

McIntyre, M. E. and Palmer, T. N.: Breaking planetary waves in the stratosphere, Nature, 305, 593–600, 1983.

Methven, J.: Potential vorticity in warm conveyor belt outflow, Quarterly Journal of the Royal Meteorological Society, 141, 1065–1071, https://doi.org/10.1002/qj.2393, 2014.

Moore, R. W. and Montgomery, M. T.: Reexamining the Dynamics of Short-Scale, Diabatic Rossby Waves and Their Role in Midlatitude Moist Cyclogenesis, Journal of the Atmospheric Sciences, 61, 754–768, 2004.

Morris, F., Robinson, C. M., Reeder, M., Schwendike, J., Parker, D. J., Bain, C. L., and Short, C. J.: Closing the Circulation Budget, Journal of Geophysical Research: Atmospheres, 130, https://doi.org/10.1029/2024jd041738, 2025.

Muñoz-Sabater, J., Dutra, E., Agustí-Panareda, A., Albergel, C., Arduini, G., Balsamo, G., Boussetta, S., Choulga, M., Harrigan, S., Hersbach, H., et al.: ERA5-Land: A state-of-the-art global reanalysis dataset for land applications, Earth system science data, 13, 4349–4383, 2021.

Parker, D. J. and Thorpe, A.: Conditional Convective Heating in a Baroclinic Atmosphere: A Model of Convective Frontogenesis, Journal of the Atmospheric Sciences, 52, 1699–1711, 1995.

Pfahl, S., Schwierz, C., Croci-Maspoli, M., Grams, C. M., and Wernli, H.: Importance of latent heat release in ascending air streams for atmospheric blocking, Nature Geoscience, 8, 610–614, https://doi.org/10.1038/ngeo2487, 2015.

Pierrehumbert, R. T. and Swanson, K. L.: Baroclinic instability, Annual review of fluid mechanics, 27, 419–467, 1995.

Raymond, D. J. and Jiang, H.: A Theory for Long-Lived Mesoscale Convective Systems, Journal of the Atmospheric Sciences, 47, 3067–3077, 1990.

Reed, R. J. and Albright, M. D.: A Case Study of Explosive Cyclogenesis in the Eastern Pacific, Monthly Weather Review, 114, 2297–2319, 1986.

Robinson, C., Narsey, S., Jakob, C., and Nguyen, H.: Weather systems associated with synoptic variability in the moist margin, Weather and Climate Dynamics, 6, 369–385, https://doi.org/10.5194/wcd-6-369-2025, 2025.

Robinson, C. M.: Synoptic dynamics of the tropical moist margin and its connection to the extratropics, Thesis, School of Earth, Atmosphere and Evnironment, 2026.

Robinson, C. M., Narsey, S., and Jakob, C.: Synoptic Variability in the Tropical Oceanic Moist Margin, Journal of Geophysical Research: Atmospheres, 129, 1–14, https://doi.org/10.1029/2024jd040814, 2024.

Saffin, L., Methven, J., Bland, J., Harvey, B., and Sanchez, C.: Circulation conservation in the outflow of warm conveyor belts and consequences for Rossby wave evolution, Quarterly Journal of the Royal Meteorological Society, 147, 3587–3610, https://doi.org/10.1002/qj.4143, 2021.

Sodemann, H.: The Lagrangian moisture source and transport diagnostic WaterSip V3.2, EGUsphere, 2025, 1–47, https://doi.org/10.5194/egusphere-2025-574, eGUsphere, 2025.

Sodemann, H., Schwierz, C., and Wernli, H.: Interannual variability of Greenland winter precipitation sources: Lagrangian moisture diagnostic and North Atlantic Oscillation influence, Journal of Geophysical Research: Atmospheres, 113, https://doi.org/10.1029/2007jd008503, 2008.

Sprenger, M. and Wernli, H.: The LAGRANTO Lagrangian analysis tool – version 2.0, Geoscientific Model Development, 8, 2569–2586, https://doi.org/10.5194/gmd-8-2569-2015, 2015.

Stan, C., Straus, D. M., Frederiksen, J. S., Lin, H., Maloney, E. D., and Schumacher, C.: Review of Tropical-Extratropical Teleconnections on Intraseasonal Time Scales, Reviews of Geophysics, 55, 902–937, https://doi.org/10.1002/2016rg000538, 2017.

Steinfeld, D. and Pfahl, S.: The role of latent heating in atmospheric blocking dynamics: a global climatology, Climate Dynamics, 53, 6159–6180, https://doi.org/10.1007/s00382-019-04919-6, 2019.

Steinfeld, D., Boettcher, M., Forbes, R., and Pfahl, S.: The sensitivity of atmospheric blocking to upstream latent heating – numerical experiments, Weather and Climate Dynamics, 1, 405–426, https://doi.org/10.5194/wcd-1-405-2020, 2020.

Teubler, F. and Riemer, M.: Dynamics of Rossby Wave Packets in a Quantitative Potential Vorticity–Potential Temperature Framework, Journal of the Atmospheric Sciences, 73, 1063–1081, https://doi.org/10.1175/jas-d-15-0162.1, 2016.

Torn, R. D.: Diagnosis of the Downstream Ridging Associated with Extratropical Transition Using Short-Term Ensemble Forecasts, Journal of the Atmospheric Sciences, 67, 817–833, https://doi.org/10.1175/2009jas3093.1, 2010.

Ullrich, P. A., Zarzycki, C. M., McClenny, E. E., Pinheiro, M. C., Stansfield, A. M., and Reed, K. A.: TempestExtremes v2.1: a community framework for feature detection, tracking, and analysis in large datasets, Geoscientific Model Development, 14, 5023–5048, https://doi.org/10.5194/gmd-14-5023-2021, 2021.

Walters, D., Baran, A. J., Boutle, I., Brooks, M., Earnshaw, P., Edwards, J., Furtado, K., Hill, P., Lock, A., Manners, J., Morcrette, C., Mulcahy, J., Sanchez, C., Smith, C., Stratton, R., Tennant, W., Tomassini, L., Van Weverberg, K., Vosper, S., Willett, M., Browse, J., Bushell, A., Carslaw, K., Dalvi, M., Essery, R., Gedney, N., Hardiman, S., Johnson, B., Johnson, C., Jones, A., Jones, C., Mann, G., Milton, S., Rumbold, H., Sellar, A., Ujiie, M., Whitall, M., Williams, K., and Zerroukat, M.: The Met Office Unified Model Global Atmosphere 7.0/7.1 and JULES Global Land 7.0 configurations, Geoscientific Model Development, 12, 1909–1963, https://doi.org/10.5194/gmd-12-1909-2019, 2019.

Wernli, H. and Gray, S. L.: The importance of diabatic processes for the dynamics of synoptic-scale extratropical weather systems – a review, Weather and Climate Dynamics, 5, 1299–1408, https://doi.org/10.5194/wcd-5-1299-2024, 2024.

Willett, M., Brooks, M., Bushell, A., Earnshaw, P., Smith, S., Tomassini, L., Best, M., Boutle, I., Brooke, J., Edwards, J. M., et al.: The met office unified model global atmosphere 8.0 and Jules global land 9.0 configurations, Geoscientific Model Development, 19, 1473–1517, 2026.

Zou, X., Cordeira, J. M., Bartlett, S. M., and Ralph, F. M.: A Case Study of an Exceptional Atmospheric River and Explosively Deepening Cyclone Over the US Central Plains in March 2019, Journal of Geophysical Research: Atmospheres, 130, https://doi.org/10.1029/2024jd042309, 2025.